npj | parkinson's disease

Article

Published in partnership with the Parkinson's Foundation

https://doi.org/10.1038/s41531-024-00715-0

Upregulated ECM genes and increased synaptic activity in Parkinson's human DA neurons with *PINK1/ PRKN* mutations

Utkarsh Tripathi[1], Idan Rosh[1], Ran Ben Ezer[1], Ritu Nayak[1], Yara Hussein[1], Ashwani Choudhary[1], Jose Djamus[1], Andreea Manole[2], Henry Houlden[3], Fred H. Gage[2] & Shani Stern[1]

Parkinson's disease (PD) is the second most prevalent neurodegenerative disease. Primary symptoms of PD arise with the loss of dopaminergic (DA) neurons in the Substantia Nigra Pars Compacta, but PD also affects the hippocampus and cortex, usually in its later stage. Approximately 15% of PD cases are familial with a genetic mutation. Two of the most associated genes with autosomal recessive (AR) early-onset familial PD are *PINK1* and *PRKN*. In vitro studies of these genetic mutations are needed to understand the neurophysiological changes in patients' neurons that may contribute to neurodegeneration. In this work, we generated and differentiated DA and hippocampal neurons from human induced pluripotent stem cells (hiPSCs) derived from two patients with a double mutation in their *PINK1* and *PRKN* (one homozygous and one heterozygous) genes and assessed their neurophysiology compared to two healthy controls. We showed that the synaptic activity of PD neurons generated from patients with the *PINK1* and *PRKN* mutations is impaired in the hippocampus and dopaminergic neurons. Mutant dopaminergic neurons had enhanced excitatory post-synaptic activity. In addition, DA neurons with the homozygous mutation of *PINK1* exhibited more pronounced electrophysiological differences compared to the control neurons. Signaling network analysis of RNA sequencing results revealed that Focal adhesion and ECM receptor pathway were the top two upregulated pathways in the mutant PD neurons. Our findings reveal that the phenotypes linked to *PINK1* and *PRKN* mutations differ from those from other PD mutations, suggesting a unique interplay between these two mutations that drives different PD mechanisms.

Parkinson's disease (PD) is a progressive neurodegenerative disease that is the second most prevalent neurological disease among the elderly[1]. PD affects approximately 2–3% of the world's population over the age of 65[2], and it is considered to be one of the aging-related diseases[3–6]. However, genetic mutations can result in an early-onset PD (before the age of 50), also known as familial PD, which accounts for 10–15% of all cases[7].

Genes involved in monogenic cases of PD include *SNCA*, which codes for the α-synuclein protein, leucine-rich repeat kinase 2 (*LRRK2*), glucosidase beta acid (GBA), phosphatase and tensin homolog (PTEN)-induced putative kinase 1 (*PINK1*), parkin RBR E3 ubiquitin-protein ligase (*PRKN*), and cytoplasmic protein sorting 35 (*VPS35*). The genes *SNCA*, *LRRK2*, and *VPS35* are associated with PD in autosomal dominant forms, whereas *PINK1* and *PRKN* are associated with PD in an autosomal recessive (AR) form ref. 8. Approximately 85% of PD cases are sporadic because no identifiable genetic etiology has been established[9].

PD is further characterized by the selective loss of the dopaminergic (DA) neurons in the substantia nigra pars compacta (SNpc)[10]. A distinguishing feature of PD is α-synuclein aggregation, which is a primary component of Lewy bodies (LBs) that contributes to the pathophysiology of various PD subtypes[11]. However, there is an ongoing debate about whether the production of α-synuclein aggregations in Lewy bodies is sufficient to cause clinical parkinsonism or neurodegeneration. A recent study has connected PD to an aberrant accumulation of several misfolded proteins, although their specific role in the disease is uncertain. While the precise pathogenic basis of PD remains unclear, several variants with variable prognoses have been extensively characterized[12].

[1]Sagol Department of Neurobiology, University of Haifa, Haifa, Israel. [2]Laboratory of Genetics, Gage, Salk Institute for Biological Studies, La Jolla, CA, USA. [3]UCL queen square institute of neurology, University College London, London, England. e-mail: sstern@univ.haifa.ac.il

Although PD is a mobility disorder in some instances, it may also impair cognition and other autonomic processes[13]. The cardinal motor symptoms include tremors, bradykinesia, hypokinesia, akinesia, stiffness, and postural instability. The current state of pharmaceutical treatment does not alter PD's normal progression. Instead, treatment focuses on symptoms and largely targets the DA system.

PINK1 and *PRKN* are the most common genes linked to AR early-onset familial PD. Disease onset typically occurs in the third or fourth decade of life and usually presents as a slow progression[14–16]. The *PRKN* gene is located on the 6q25.2–27 chromosome[17] and encodes the Parkin protein, a cytosolic E3 ubiquitin ligase that functions in the ubiquitin-proteasome pathway. PD onset in people with *PRKN* mutations occurs before the fourth decade of life, constituting 50% of all AR PD cases. These mutations range from minor deletions and base pair substitutions to massive deletions that span hundreds of nucleotides[18,19].

Following *PRKN*, the second most frequent AR mutation in young-onset PD is *PINK1*, a serine/threonine protein kinase encoded by the *PINK1* gene. *PINK1* has a kinase domain at the C- terminus and a mitochondrial targeting domain at the N-terminus. The proteasome truncates the N-terminal domain of the gene, resulting in the release of cytosolic *PINK1*[20]. Forty-two different mutations have been documented within the *PINK1* exons in both heterozygous and homozygous states, with Q456X being the most common form of *PINK1*-related PD mutation[21,22]. Recent studies using human induced pluripotent stem cells (hiPSCs) have shown that *PINK1* and *PRKN* mutations are involved in mitochondrial dysfunction and that *PINK1* and *PRKN* cooperate to regulate mitophagy, one of the mitochondrial quality control mechanisms[23,24].

The primary pathogenic symptom of PD is the loss of DA neurons, so the study of PD using hiPSCs focuses on DA neuronal differentiation[25,26]. Previous studies that worked on phenotypic characterization using hiPSCs became the platform to establish new paradigms for cellular therapeutic techniques, drug development, and preclinical and clinical study screening[27–34]. In hiPSC-derived DA neurons, mutant *PRKN* failed to associate with *PINK1*, which in turn reduced dopamine vesicle endocytosis, disrupted microtubule stability, decreased neuronal complexity, increased spontaneous excitatory post-synaptic currents in neurons, and increased dopamine release (although there is still no consensus on this specific point). Mutant *PINK1* increased mitochondrial DNA levels, mitochondrial oxidative stress, autophagy, and mitochondrial respiration while interfering with ubiquitin-mediated autophagy in the mitochondria and lysosomes[35,36].

In this study, we generated and differentiated DA neurons from hiPSCs derived from two patients with a double mutation in their *PRKN* (heterozygous) and *PINK1* (one patient with a homozygous mutation and the other with a heterozygous mutation) genes and compared their electrophysiological measures to DA neurons derived from two control hiPSC lines. Although PD is considered a movement disorder, many patients also experience non-motor symptoms, including depression and cognitive decline[37]. Changes in the hippocampus have been found that are related to these symptoms[38]. Furthermore, as the hippocampus region is the brain's stem cell niche, previous data indicate that genetic abnormalities in PD patients may influence adult hippocampal neurogenesis[39]. Therefore, we also differentiated hippocampal neurons from the same patients and the two controls to measure the changes in hippocampal neurons[40].

We employed electrophysiological techniques to study neurophysiological changes in DA and hippocampal neurons derived from PD patients. We found that *PINK1* and *PRKN* mutant DA neurons showed increased synaptic activity compared to control neurons. This finding was in contrast to all our measurements in DA neurons derived from patients with other mutations and sporadic PD[41]. Interestingly, the patient DA neurons harboring the homozygous *PINK1* mutation (with heterozygous *PRKN*) showed a more severe abnormality than the patient DA neurons harboring the heterozygous *PINK1* mutation (with heterozygous *PRKN*), suggesting the importance of the mutant gene dosage. Additionally, while in our previous study[41], the reduction in synaptic activity was accompanied by down-regulation of genes related to the brain extracellular matrix (ECM) and focal adhesions, in this study we saw an up-regulation of these pathways, suggesting a connection between the expression of genes from the ECM and focal adhesion pathways and synaptic activity. The hippocampal dentate gyrus (DG) granule neurons derived from the patients with the *PINK1* and *PRKN* mutations showed a different phenotype, suggesting that PD may have a different effect on neurons from different brain areas.

Results

DA neurons from patients with *PINK1* and *PRKN* mutations exhibited alterations in their sodium and potassium currents compared to healthy controls

Our study included two hiPSC lines derived from healthy controls (a 71-year-old male and a 53-years old male) and two PD hiPSC lines that were derived from patients with *PINK1* and *PRKN* mutations: a 48-year-old patient (female) with a homozygous *PINK1* and heterozygous *PRKN* mutation and a 75-year-old patient (male) with a heterozygous *PINK1* and heterozygous *PRKN* mutation (Supplementary Table 4 gives detailed information about mutations). We differentiated these hiPSCs into DA neurons (see Materials and Methods) and examined the intrinsic characteristics and synaptic activity of the neurons using a whole-cell patch clamp.

A total of 58 control and 41 *PINK1* and *PRKN* mutant neurons (23 neurons from the homozygous *PINK1* patient and 18 neurons from the heterozygous *PINK1* patient) were patched between 7 and 10 weeks post-differentiation. Figure 1o shows immunostaining with MAP2 (red), which marks mature neurons, and tyrosine hydroxylase (TH green), which marks dopaminergic neurons along with DAPI. Supplementary Fig. 3a shows the percentage of TH + /MAP2+ neurons (90.5 ± 2% in controls and 90 ± 4% in *PINK1* and *PRKN* mutant neurons) and also the percentage of GIRK2 + / MAP2+ neurons (82 ± 4% in controls and 81 ± 4% in *PINK1* and *PRKN* mutant neurons). Supplementary Fig. 3b shows the percentage of astrocytes (5 ± 1% in control cultures, 7 ± 4.5% in *PINK1* and *PRKN* mutant cultures stained by GFAP) in our DA neurons culture. Figure 1a, b show a representative picture of evoked potentials in a control neuron and a *PINK1* and *PRKN* mutant neuron. The total number of evoked potentials in the first 32 depolarization steps (see Methods) was not significantly different in the *PINK1* and *PRKN* neurons compared to the control neurons (Fig. 1c). However, when we analyzed the recordings from the neurons with the homozygous and heterozygous *PINK1* mutation (and a *PRKN* mutation) separately, we found that the homozygous line had a significantly larger number of evoked potentials compared to the control (Supplementary Fig. 2a, homozygous *PINK1* mutant vs. control $p = 0.03$). This finding provides evidence that the homozygous mutation that also causes an earlier disease onset (see Methods) has more severe phenotypes. Figure 1d, e shows an example of a single evoked potential of control and *PINK1* and *PRKN* mutant neurons. The fast AHP (Afterhyperpolarization) (5 ms, see Methods) was not significantly different in *PINK1* and *PRKN* mutant neurons in comparison to the control neurons (Fig. 1f). The spike amplitude and spike threshold were not significantly different in *PINK1* and *PRKN* mutant neurons compared to control neurons (Fig. 1g, h). The cell capacitance was significantly higher in *PINK1* and *PRKN* mutant neurons compared to control neurons (Fig. 1i, $p < 0.0001$). Figure 1j, k shows examples of the sodium and potassium currents recordings obtained in the voltage-clamp mode of control and *PINK1* and *PRKN* mutant neurons, respectively. The sodium currents (between −20 mV to 0 mV, see Methods) were significantly decreased (Fig. 1l, $p = 0.0025$) in *PINK1* and *PRKN* mutant neurons compared to control neurons. In contrast, both the fast potassium and slow potassium currents were significantly larger (between 40 mV to 80 mV) in *PINK1* and *PRKN* mutant neurons compared to the control neurons (Fig. 1m, $p = 0.08$ and 1(n), $p = 0.012$) with 1-way ANOVA analysis.

Increased synaptic activity was observed in DA neurons derived from PD patients with *PINK1* and *PRKN* mutations compared to control neurons

Next, we compared the synaptic activity between control and *PINK1* and *PRKN* mutant neurons. Figure 2a, b shows examples of excitatory post-

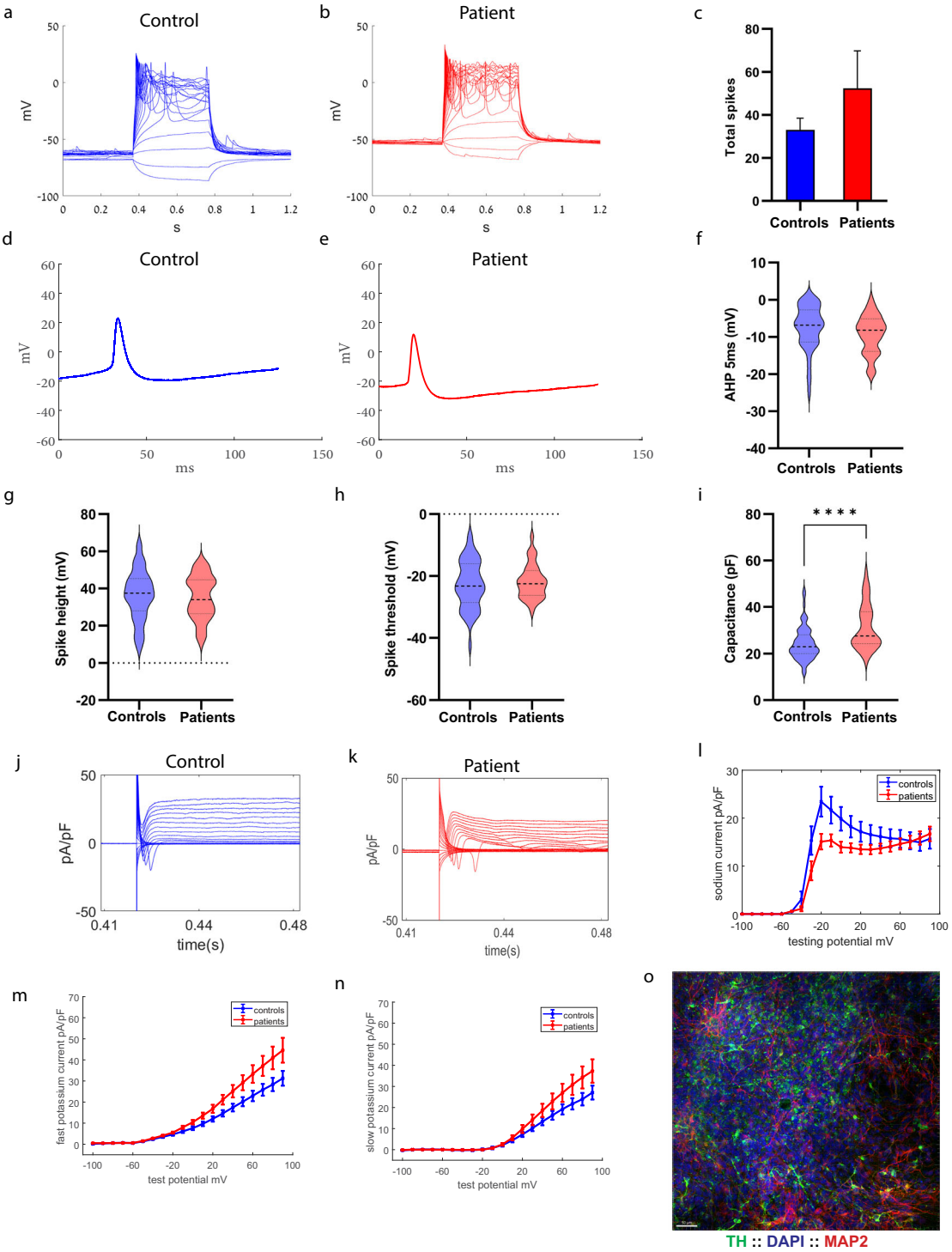

Fig. 1 | Patient-derived DA neurons exhibited increased potassium currents compared to control neurons. A representative evoked action potential trace in (**a**) control DA neurons and (**b**) DA *PINK1* and *PRKN* mutant neurons. **c** The total evoked potential was not significantly different between control and *PINK1* and *PRKN* mutant neurons. A representative picture of the spike shape of (**d**) control and (**e**) *PINK1* and *PRKN* mutant neurons. **f** The 5 ms AHP was not different in neurons derived from PD patients with *PINK1* and *PRKN* mutations compared to control neurons. **g** The spike height was significantly smaller in neurons derived from PD patients with *PINK1* and *PRKN* mutations compared to healthy controls. Other spike shape features, i.e., **h** spike threshold and **i** capacitance, were not significantly different between patient-derived DA neurons and control neurons. Representative recordings of sodium and potassium currents in (**j**) control neurons and (**k**) *PINK1* and *PRKN* mutant neurons. **l** Sodium current, **m** fast potassium currents, and **n** slow potassium currents were significantly increased in patient-derived DA neurons using a one-way ANOVA analysis. **o** DA neurons were characterized in culture using immunohistochemistry; Tyrosine Hydroxylase (TH) (green) specifically marks DA neurons in the culture (Scale bar 50 µm), DAPI (blue) stains nuclei, and MAP2 (red) marks neurons. The percentage of TH-positive neurons out of the MAP2-positive neurons is shown in Supplementary Fig. 3a and was 90.5 ± 1.9 in controls and 90 ± 4.2% in *PINK1* and *PRKN* mutant neurons. Unless otherwise noted, the error bars in this and the following figures indicate the standard error. Asterisks in this figure denote statistical significance as indicated by the following codes: $^{*}p < 0.05$, $^{**}p < 0.01$, $^{***}p < 0.001$, $^{****}p < 0.0001$.

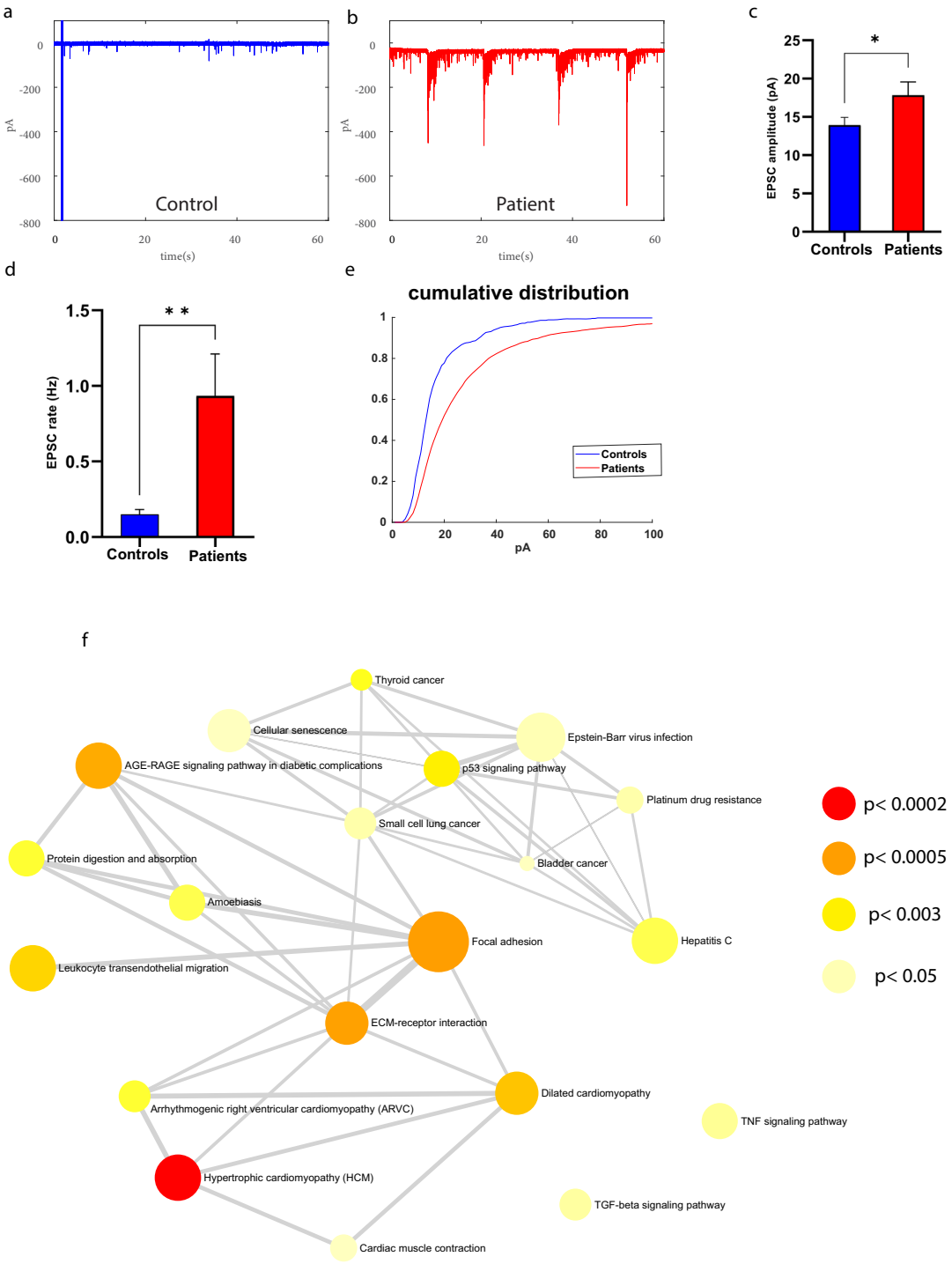

Fig. 2 | Patient-derived DA neurons exhibited increased synaptic activity compared to control neurons. Example recordings of EPSCs in (**a**) control DA neurons and (**b**) DA *PINK1* and *PRKN* mutant neurons. **c** EPSC average amplitude was significantly larger in *PINK1* and *PRKN* mutant neurons compared to control neurons. **d** DA *PINK1* and *PRKN* mutant neurons showed significantly increased EPSC rates compared to control neurons. **e** The cumulative distribution of EPSC amplitudes was right shifted for *PINK1* and *PRKN* mutant neurons, indicating higher EPSC amplitudes than for control neurons. **f** Dysregulated pathways in *PINK1* and *PRKN* mutant DA neurons compared to healthy controls at 7–8 weeks post differentiation. Signaling network analysis with the top enriched KEGG pathways for the *PINK1* and *PRKN* patient-derived neurons compared to the controls shows that the top dysregulated pathways for this double mutation are "ECM receptor interaction" and "Focal adhesion." The red circle indicates a significantly up-regulated gene and the green indicates a significantly down-regulated gene (FDR < 0.05). Asterisks in this figure denote statistical significance as indicated by the following codes: $^{*}p < 0.05$, $^{**}p < 0.01$, $^{***}p < 0.001$, $^{****}p < 0.0001$.

synaptic currents (EPSCs) in control and *PINK1* and *PRKN* mutant neurons. The mean amplitude of EPSCs was significantly increased in *PINK1* and *PRKN* mutant neurons compared to the control neurons (Fig. 2c, $p = 0.04$). In addition, the EPSC rate was significantly increased in *PINK1* and *PRKN* mutant neurons compared to control neurons (Fig. 2d, $p = 0.001$). Further, when we separately analyzed the synaptic activity of the homozygous and heterozygous *PINK1* mutant neurons, we found that the homozygous *PINK1* mutant neurons had a more increased EPSC rate (homozygous *PINK1* mutant vs. control: $p = 0.0002$, control vs. heterozygous *PINK1* mutant: $p = 0.02$, Supplementary Fig. 2b) and also increased

EPSC amplitude (homozygous PINK1 mutant vs. control: $p = 0.01$, Supplementary Fig. 2c) compared to control neurons. The EPSC rate was not significantly different between the heterozygous *PINK1* mutant and control neurons (Supplementary Fig. 2b). Figure 2e shows the cumulative distribution of EPSC amplitude of *PINK1* and *PRKN* mutant and control neurons. The cumulative distribution of *PINK1* and *PRKN* mutant neurons' EPSC amplitude was right-shifted compared to control neurons, indicating higher EPSC amplitudes.

ECM and focal adhesion genes are upregulated in *PINK1* and *PRKN* mutant neurons compared to healthy controls

RNA was extracted from DA neurons derived from two *PINK1* and *PRKN* mutant PD patients and two control individuals, and gene expression differences were analyzed. There were a total of 1834 differentially expressed genes (DEGs); specifically, 1,150 upregulated and 684 downregulated genes were identified in the *PINK1* and *PRKN* mutant DA neurons compared to healthy controls (Supplementary Table 2a–c) (|log2 fold change|> 1.1, FDR < 0.05). When examining just the homozygous mutation, there were 677 upregulated genes and 438 downregulated genes; in total, there were 1115 DEGs found in the homozygous *PINK1* mutant DA neurons compared to healthy controls (Supplementary Table 3a–c). The signaling network analysis with the top enriched KEGG pathways for the *PINK1* and *PRKN* mutant DA neurons compared to the controls is presented in Fig. 2f. The ECM receptor interaction and focal adhesion pathways were significantly upregulated pathways in *PINK1* and *PRKN* mutant DA neurons (supplementary Table 1a) compared to healthy controls, whereas these pathways were significantly dysregulated in homozygous *PINK1* mutant DA neurons (supplementary Tig. 2d, supplementary Table 1b). In the Gene Ontology (GO) enrichment analysis, significant upregulation was found in the extracellular matrix structural constituent molecular function in both homozygous and heterozygous *PINK1* and *PRKN* mutant DA neurons (Supplementary Table 1c, d). Concurrently, a substantial upregulation was also observed in several cellular components associated with the ECM in *PINK1* and *PRKN* mutant as well as in the homozygous *PINK1* mutant DA neurons (Supplementary Table 1e, f). The ECM receptor interaction pathway is involved in the regulation of synaptic plasticity[42,43]. The focal adhesion proteins maintain the adhesion of brain cells to the ECM and are essential for neuronal migration and neurogenesis[44,45]. Additionally, many biological procedures related to brain development and neurogenesis were significantly downregulated in GO enrichment analysis of combined *PINK1* and *PRKN* mutant as well as only homozygous *PINK1* mutant DA neurons (Supplementary Table 1g, h).

Hippocampal neurons derived from patients with the *PINK1* and *PRKN* mutations are hypoexcitable with reduced synaptic activity

We next differentiated hippocampal neurons from the PD patients with the *PINK1* and *PRKN* mutations and performed electrophysiology to compare them to healthy controls. A total of 13 control and 18 *PINK1* and *PRKN* mutant hippocampal neurons were patched at the first time point, 29 control and 20 *PINK1* and *PRKN* mutant hippocampal neurons at the second time point, and 12 control and 10 *PINK1* and *PRKN* mutant hippocampal neurons at the third time point. Figure 3p shows immunostaining for hippocampal neurons using MAP2 (red) to mark mature neurons and PROX1 (green) to mark DG granule neurons along with DAPI in blue. Supplementary Fig. 3c shows the percentage of PROX1 + /MAP2+ neurons in immature cultures (first-time point|) (73 ± 2.5 in control immature neurons and 73.5 ± 6 in *PINK1* and *PRKN* mutant immature neurons) and also shows the percentage of PROX1+/MAP2+ neurons in mature cultures (second-time point) (70 ± 2.5 in control mature neurons and 73 ± 7 in *PINK1* and *PRKN* mutant mature neurons). Figure 3a, b presents a representative image of evoked potentials in control and *PINK1* and *PRKN* mutant hippocampal neurons at the second time point. The total number of evoked potentials in the first 30 depolarization steps was not significantly different in control and PINK1 and *PRKN* mutant hippocampal neurons (Fig. 3c). Figure 3d, e shows representative traces of EPSCs in control and *PINK1* and *PRKN* mutant hippocampal neurons. The average amplitude of EPSCs per recorded cell was significantly lower in *PINK1* and *PRKN* mutant hippocampal neurons compared to control neurons at the second time point (Fig. 3f, $p = 0.0056$); there was no significant difference at earlier and later time points (Supplementary Fig. 1c, i). The rate of synaptic events was decreased in *PINK1* and *PRKN* mutants compared to control neurons at the second time point (Fig. 3g, $p = 0.0055$, using the Mann–Whitney test) and the first time point (Supplementary Fig. 1b); whereas the synaptic rate was not different at the third time point (Supplementary Fig. 1h). The cumulative distribution of the amplitudes of EPSCs in *PINK1* and *PRKN* mutant hippocampal neurons was shifted towards the left compared to control neurons, indicating smaller amplitudes at the second time point (Fig. 3h); there was no shift at the first and third time point (Supplementary Fig. 1d, j). Figure 3i, j shows representative traces of an action potential of control and *PINK1* and *PRKN* mutant hippocampal neurons. The fAHP (5 ms, see Methods) was not significantly different between control neurons and *PINK1* and *PRKN* mutant hippocampal neurons at the second time point (Fig. 3k). However, *PINK1* and *PRKN* mutant hippocampal neurons had decreased fAHP compared to control neurons when they were in the early maturation period (first time point) (Supplementary Fig. 1a); it was not significantly different when they matured (third time point, Supplementary Fig. 1g). Figure 3l, m represents the traces of the sodium and potassium currents acquired in the voltage-clamp mode of control hippocampal and *PINK1* and *PRKN* mutant hippocampal neurons, respectively. *PINK1* and *PRKN* mutant hippocampal neurons that were recorded at the second time point post-differentiation did not show any significant differences in sodium or potassium currents (Fig. 3n, o).

PINK1 and *PRKN* mutant hippocampal neurons had slightly reduced slow potassium currents at the first time point (not significant, Supplementary Fig. 1e). However, the slow potassium current was significantly increased in *PINK1* and *PRKN* mutant hippocampal neurons compared to control neurons at the third time point ($p = 0.03$, Supplementary Fig. 1k). In addition, the sodium current was significantly decreased in *PINK1 and PRKN* mutant hippocampal neurons at the first time point ($p = 0.0002$, Supplementary Fig. 1f) but significantly increased in *PINK1* and *PRKN* mutant hippocampal neurons compared to control neurons as they matured (third time point, $p = 0.0003$, Supplementary Fig. 1l).

DG hippocampal neurons derived from patients with the *PRKN* and *PINK1* mutations demonstrated an increased rate of calcium transients compared to control neurons

We also measured the calcium transients (see Methods) in DG hippocampal neurons derived from healthy individuals and *PINK1* and *PRKN* mutant patients. Figure 4a shows a fluorescent image of control hippocampal neurons after incubation with fluo-5 calcium indicator. Figure 4b shows calcium transient activity (fluorescence intensity in different regions of interest (ROIs) corresponding to the ROIs in Fig. 4a. We observed very synchronous activity between some neurons in a few recordings of heterozygous *PINK1* mutant neurons. To obtain a measure of the connectivity, we calculated the mean correlation (See Methods) between neurons and compared the top five ROIs with the most correlated neurons to compare the heterozygous *PINK1* mutant and control neuronal networks. The mean correlation was significantly increased in heterozygous *PINK1* mutant neurons compared to control neurons (Fig. 4e, $p = 0.035$). Figure 4c, d shows an illustration of the correlation heat maps of the most correlated neurons in control and *PINK1* and *PRKN* mutant neuronal networks. Figure 4f, g represents fluorescent images of control *PINK1* and *PRKN* mutant hippocampal neurons. These results indicate that, at the second time point, the *PINK1* and *PRKN* mutant neuronal network was more connected and synchronized than the control neuronal network.

Additionally, we found that some neurons exhibited high-frequency firing in the heterozygous *PINK1* mutant neuronal networks. Therefore, we compared the power spectral density (PSD) of the five areas with the highest average frequency in the control and

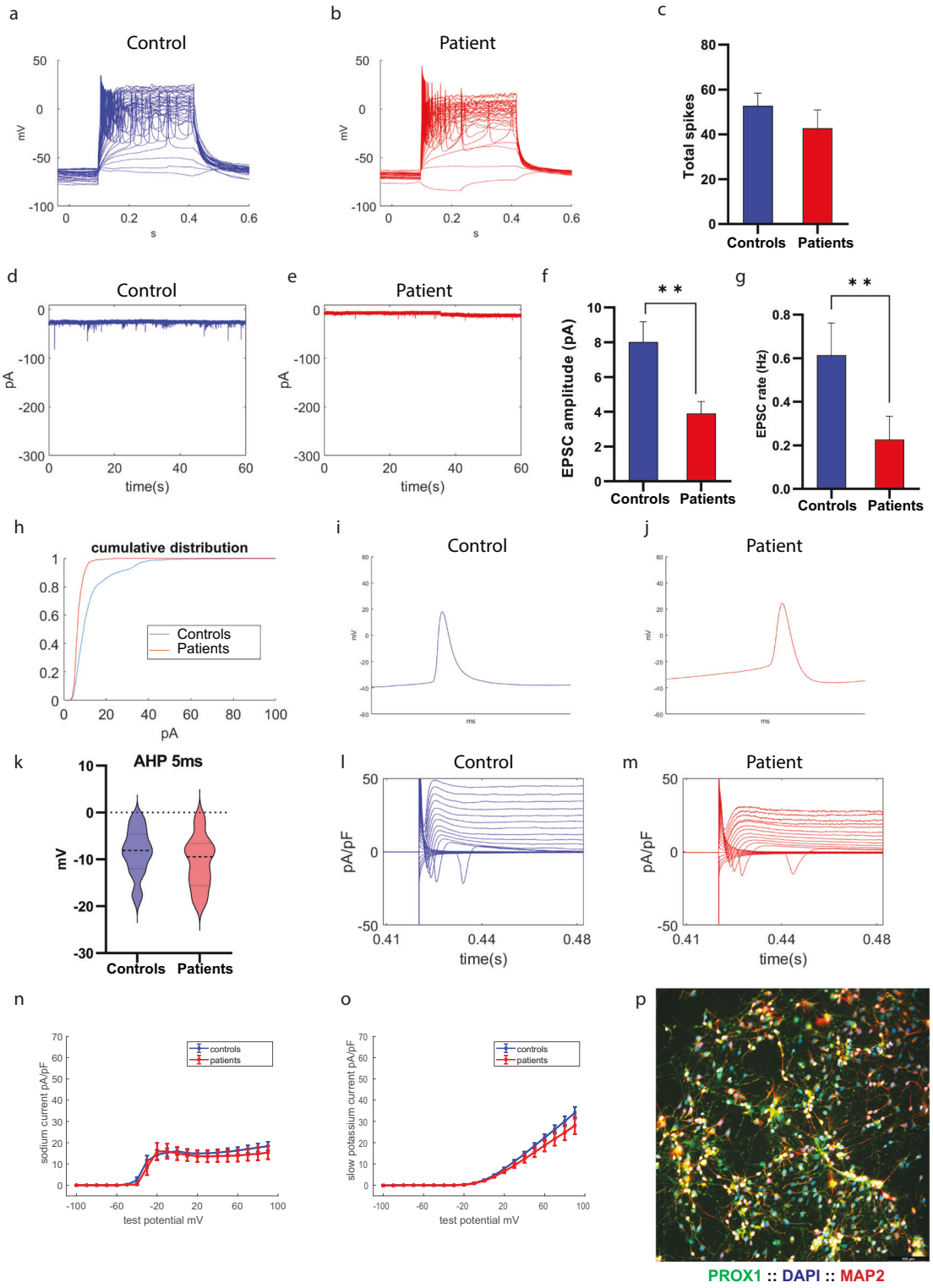

heterozygous *PINK1* mutant neuronal network. Figure 4h, i presents control and heterozygous *PINK1* mutant neurons with a high calcium transient event frequency. We calculated the ratio of area under the PSD curves of these fluorescent signals for the entire frequency spectrum divided by the higher frequency component (see Methods). Heterozygous *PINK1* mutant neurons had a significantly higher ratio compared to control neurons (Fig. 4j, $p = 0.01$), which shows that the heterozygous *PINK1* mutant neuronal networks are fast oscillatory behaving neurons compared to the control neuronal network.

We performed calcium imaging at two different time points for hippocampal neurons. Figure 4k, m shows illustrative calcium transient time series plots for control and *PINK1* and *PRKN* mutant neurons at two different time points. Figure 4k, l corresponds to 2–4 weeks post-differentiation. Figure 4m, n corresponds to 6-7 weeks post-differentiation. The dynamics of calcium waves in astrocytes are usually reported as being very slow in nature[46–48]. We used these dynamics to classify astrocyte activity in the culture (see Methods). Astrocytes' average fluorescence ratio (see Methods) was increased for control neurons compared to

Fig. 3 | Patient-derived hippocampal neurons possessed reduced excitatory post-synaptic activity compared to healthy controls. Representative evoked action potential traces in (**a**) control hippocampal neurons and (**b**) hippocampal *PINK1* and *PRKN* mutant neurons. **c** The total number of evoked potentials was not significantly different between control and *PINK1* and *PRKN* mutant neurons. Example recordings of EPSCs in (**d**) control hippocampal neurons and (**e**) hippocampal *PINK1* and *PRKN* mutant neurons. **f** The EPSC amplitude was significantly reduced in *PINK1* and *PRKN* mutant neurons compared to control neurons. **g** Hippocampal *PINK1* and *PRKN* mutant neurons showed significantly reduced EPSC rates compared to control neurons. **h** The cumulative distribution of EPSC amplitudes showed that EPSC amplitudes of *PINK1* and *PRKN* mutant neurons were left-shifted compared to control neurons, indicating smaller EPSC amplitudes in hippocampal *PINK1* and *PRKN* mutant neurons. A representative trace of the spike shape of (**i**) control and (**j**) *PINK1* and *PRKN* mutant neurons. **k** The 5 ms AHP was not significantly different in *PINK1* and *PRKN* mutant neurons compared to control neurons. Representative recordings of sodium and potassium currents in (**l**) control neurons and (**m**) *PINK1* and *PRKN* mutant neurons. **n** Fast potassium currents and **o** slow potassium currents were not significantly different in patient-derived hippocampal neurons compared to controls. **p** Characterization of hippocampal neurons in culture with immunohistochemistry. PROX1 (blue) marks dentate gyrus granule neurons (Scale bar 30 μm). The percentage of PROX1-positive neurons out of the MAP2 positive neurons in immature and mature cultures is shown in Supplementary Fig. 3c and was (73.30 ± 2.49 in control immature neurons and 73.54 ± 5.66 in *PINK1* and *PRKN* mutant immature neurons. In the mature neurons (second time point), the percentage of PROX1-positive neurons was 70.08 ± 2.46 in control mature neurons and 72.86 ± 6.73 in *PINK1* and *PRKN* mutant mature neurons. Asterisks in this figure denote statistical significance as indicated by the following codes: $*p < 0.05$, $**p < 0.01$, $***p < 0.001$, $****p < 0.0001$.

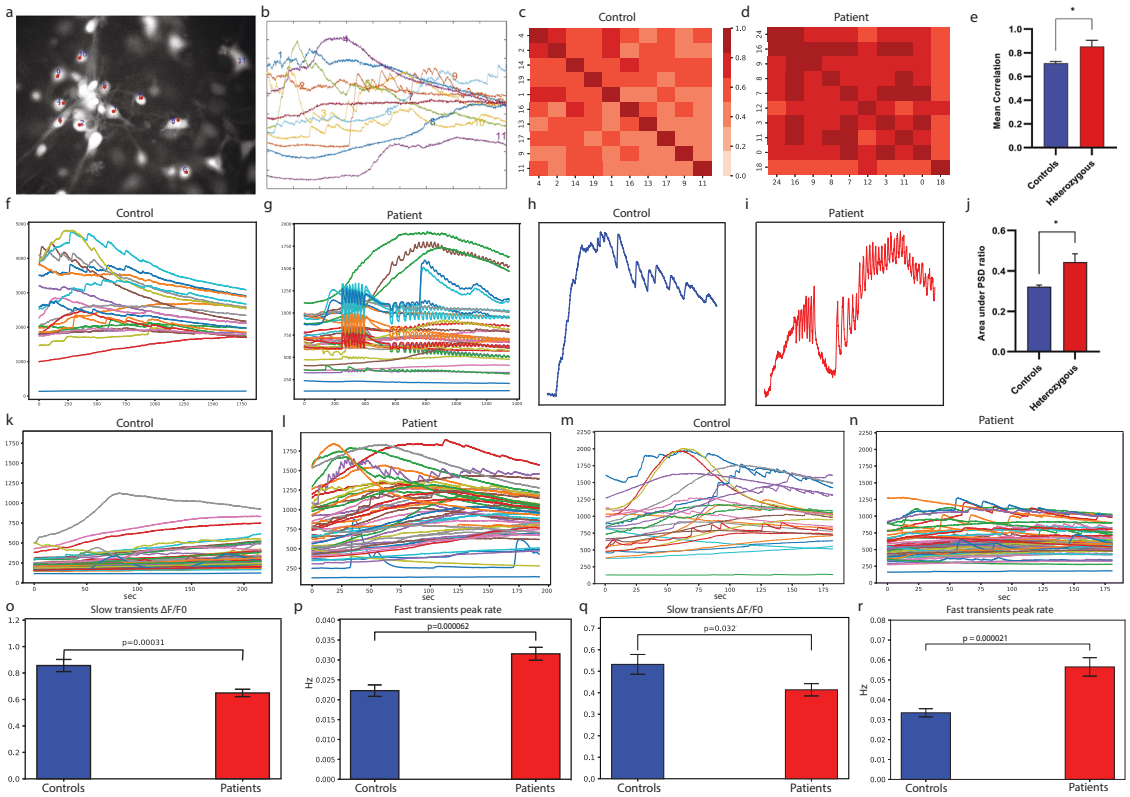

Fig. 4 | Calcium transient activity was increased and more synchronized in hippocampal neurons harboring *PINK1* and *PRKN* mutations compared to healthy controls. a A sample video frame of a calcium imaging recording. Red marks represent neurons marked as the region of interest. **b** The corresponding fluorescence time series plot for all marked neurons in **a**. An example heatmap of the mean correlation value of area recorded area from (**c**) control hippocampal DG granule neuron network and (**d**) hippocampal DG granule neuron network with *PINK1* and *PRKN* mutation. **e** The average correlation in the top correlated areas (see Methods) of hippocampal DG granule neuron cultures with *PINK1* and *PRKN* mutations was larger compared to control neuronal culture. Representative areas of (**f**) control hippocampal DG granule neurons culture and (**g**) hippocampal DG granule neurons culture with *PINK1* and *PRKN* mutation with high synchronous activity. The *PINK1* and *PRKN* mutant neuronal cultures exhibited high synchrony. Representative calcium transient time series plot with a high event frequency of (**h**) a control hippocampal DG granule neuron and (**i**) a hippocampal DG granule neuron with *PINK1* and *PRKN* mutation. The *PINK1* and *PRKN* mutant neuronal cultures exhibited high-frequency firing patterns. **j** The top 5 ratio of area under the power spectral density curve of such fluorescent signals between the whole frequency spectrum and higher frequency components was larger in *PINK1* and *PRKN* mutant neurons compared to controls. **k**–**n** A representative plot of fluorescence transients at the first time point (**k**) in control neurons and (**l**) in *PINK1* and *PRKN* mutant neurons. Examples for the second time point are shown in (**m**) for controls and (**n**) for *PINK1* and *PRKN* mutant neurons. The second time point. Increased activity can be observed in the mutant neurons, and higher synchrony can be observed in the mutant neurons in the second time point. At the first time point of calcium imaging (**o**), the average astrocytes fluorescence ratio Δf/fo (see Methods) was significantly decreased in hippocampal *PINK1* and *PRKN* mutant neurons, whereas (**p**) the calcium fast transients' event (attributed to the neurons) rate was increased in hippocampal *PINK1* and *PRKN* mutant neurons. At the second time point of calcium imaging (**q**), the average astrocytes fluorescence ratio Δf/fo was significantly lower in hippocampal *PINK1* and *PRKN* mutant neurons, and (**r**) the calcium fast transient event rate (attributed to the neurons) was higher in neurons of hippocampal *PINK1* and *PRKN* mutant neurons. Asterisks in this figure denote statistical significance as indicated by the following codes: $*p < 0.05$, $**p < 0.01$, $***p < 0.001$, $****p < 0.0001$.

PINK1 and *PRKN* mutant neurons during the first time point of calcium imaging (Fig. 4o, $p = 0.0003$) and also at the second time point of calcium imaging (Fig. 4q, $p = 0.03$). The calcium transient event rate in neurons was significantly higher in hippocampal *PINK1* and *PRKN* mutant neurons at the first time point of calcium imaging (Fig. 4p, $p = 0.00006$). *PINK1* and *PRKN* mutant hippocampal neurons exhibited increased calcium transient event rates even after maturation (second time point of calcium imaging, Fig. 4r, $p = 0.00002$).

Discussion

Genetic mutations in *PRKN*, *PARK7*, and *PINK1* are among the well-known familial mutations contributing to PD[49]. Mutations in *PINK1* and *PRKN*[36] have been causally connected to early-onset PD. Previous studies have documented the α-synuclein-mediated pathophysiology in PD as a six-stage process[50]. In stage 3 of the pathology, loss of DA neurons in the substantia nigra causes motor symptoms (tremor, bradykinesia, and stiffness) that can be evaluated for clinical diagnosis. During stage 4, Lewy pathology affects the hippocampus, causing cognitive dysfunction that progresses to the cortex, causing dementia in later stages[51]. Given this clinical and pathological progression of PD, we investigated both dopaminergic and hippocampal neurons differentiated from PD patient-derived hiPSCs. Initial studies on hiPSCs of *PINK1* and *PRKN* mutations have found mitochondrial defects and α-synuclein accumulation[24]. Here, we investigated the functional properties of hiPSC-derived DA neurons from a patient with homozygous *PINK1* and heterozygous *PRKN* mutation and another patient with heterozygous mutation in the *PINK1* and the *PRKN* genes. The DA neurons of the patients were compared to DA neurons from healthy individuals. In the combined electrophysiological analysis of DA derived from the PD patients (both homozygous and heterozygous *PINK1* mutant with heterozygous *PRKN* mutation), we did not observe a significant difference in the number of evoked action potentials in response to current stimulation compared to healthy controls. Interestingly, when we separated the neurons derived from the patient with the homozygous mutation in the *PINK1* gene, these neurons were significantly hyperexcitable. Importantly, the patient with the homozygous mutation developed PD at a much earlier age. We further investigated the synaptic activity in *PINK1* and *PRKN* mutant DA neurons and found that the synaptic activity was drastically increased in the *PINK1* and *PRKN* mutant neurons compared to the healthy control neurons. Comparing the synaptic activity between the two *PINK1* and *PRKN* mutant lines showed that the neurons derived from the homozygous patient had a more robust phenotype. Supporting this finding, a previous electrophysiological study of corticostriatal neurons in mice showed differences in synaptic plasticity of corticostriatal neurons with a homozygous *PINK1* mutation and a heterozygous mutation[52,53]. In line with these findings, differences in synaptic plasticity (both long-term potentiation and long-term depression) were observed during whole-cell recordings in slices of a rodent model of PD with different levels of dopamine denervation, which was induced with different doses of 6-Hydroxydopamine hydrochloride nigrostriatal injection[54].

Overall, we could detect alterations in electrophysiological properties in *PINK1* and *PRKN* mutant DA neurons that were distinctly stronger in the neurons derived from the patient with the homozygous mutation. A recent study with DA neurons derived from two patients with a *PRKN* mutation showed a reduction in synaptic activity[41]. In the current study, we observed increased synaptic activity, which may indicate some interaction between the two mutations in the *PINK1* and *PRKN* genes and their functional pathways. The high synaptic activity in spiny projection neurons (SPN) has been previously shown in animal PD models[55]. Researchers using mice carrying the knockin mutations *LRRK2-G2019S* or *D2017A* (kinase-dead) showed that, compared to wild-type SPNs, *G2019S* SPNs in postnatal day 21 mice showed a four-fold increase in sEPSC frequency during whole-cell recordings on slices. Through excitotoxicity mechanisms, the high synaptic activity and hyperexcitability of *PINK1* and *PRKN* mutant DA neurons may contribute to neurodegeneration and synaptic loss. A previous study observed activity-dependent degeneration in GABAergic synapses in the hippocampal culture from presynaptic protein knockout mice[56]. This elevated synaptic activity in dopaminergic *PINK1* and *PRKN* mutant neurons seems paradoxical, as PD is usually associated with synaptic loss[41,57,58]. However, it is possible that biphasic synaptic activity (initially elevated synaptic activity and then decreased synaptic activity at a later time) alterations occur in these mutations, just as previously found in Alzheimer's disease (AD), another disease characterized by severe neurodegeneration[59], and also in autism models[27,60]. It is important to note that the patient with the homozygous *PINK1* mutation was a female, whereas the other patient and the controls were males. Sex can contribute to the variability in clinical presentation, disease progression, and response to treatment in PD patients. In general, men have a higher risk of developing PD, and some studies have shown sex differences in the clinical features and progression of the disease[61], and the differences in human neurons derived from females and males have still not been investigated.

Furthermore, we performed transcriptomic analysis of the hiPSC-derived DA neurons to understand the dysregulated biological pathways and underlying mechanisms related to these double mutations. The ECM receptor interaction and focal adhesion pathways were identified as significantly upregulated in the DA neurons derived from the PD patients with the *PINK1* and *PRKN* mutations. ECM receptor proteins (e.g., integrins) have been reported to play an essential role in developing neuronal structure and signaling mechanisms during synaptic interaction[42]. Both neurodegenerative diseases like AD and neuropsychiatric diseases, including schizophrenia, autism spectrum disorders, and depression, have been linked to ECM protein dysregulation[62–66]. Similarly, focal adhesion proteins are essential in linking ECM proteins to the cytoskeletal elements[67] and are also known to be critical in AD pathogenesis[68]. These two pathways may interact to regulate crucial signaling mechanisms during synaptic connectivity, which relates to the abnormal synaptic activity observed in *PINK1* and *PRKN* mutant DA neurons. Dysregulation of ECM receptor proteins and focal adhesion proteins has also been reported recently from DA neurons derived from several PD-related mutations and sporadic patients[41]. Interestingly, in that study, ECM and focal adhesion-related genes were down-regulated, and the synaptic activity was also decreased, whereas in this study, these pathways are upregulated, yet the synaptic activity is also increased. This finding suggests a link between ECM and focal adhesion pathways and synapse formation.

In our transcriptomic analysis, 97 key mitochondrial genes such as *ACAD8*, *AFG3L2*, *AMT*, *BID*, *CYP11A1*, *DLD*, *MTERF4*, *MTFR1*, *UQCC2*, *MT-ND1*, and *MT-ND2* were identified as differentially expressed in *PINK1* and *PRKN* mutant DA neurons compared to healthy controls. For example, *ACAD8* (upregulated), which is involved in fatty acid metabolism, can impact mitochondrial energy production[69]. *AFG3L2* (downregulated), a gene associated with mitochondrial complex assembly, has implications in mitochondrial dysfunction and has been shown to be essential for axonal development[70]. Upregulation of the *GLS* gene, which catalyzes the conversion of glutamine to glutamate[71], could be linked to altered glutamatergic signaling, potentially contributing to neuronal hyperexcitability[72]. In addition, excess glutamate leads to oxidative stress and neuronal injury, termed as excitotoxicity[73]. *BID* (upregulated), a pro-apoptotic molecule, could be linked to mitochondria-mediated apoptosis[74]. *MT-ND1* (upregulated) and *MT-ND2* (upregulated) are mitochondria-encoded subunits of complex I, which are essential for mitochondrial respiration, and have been linked to neurodegeneration[75]. *DHRS7B* is downregulated and is associated with redox homeostasis, aligning with the concept of increased oxidative stress in these neurons. The differential expression of many such genes, exemplified by those mentioned,, along with the observed enrichment of GO terms related to organelles and intracellular membranes, suggests a significant impact on mitochondrial function and integrity. The overly active *PINK1* and *PRKN* mutant neurons probably require more energy, which in turn activates and causes dysregulation of mitochondrial genes (or vice versa); this in turn increases metabolic rate and oxidative stress, contributing to neurodegeneration eventually. Our data, therefore suggest more evidence for mitochondrial impairment as a hallmark of PD, possibly through associations with neuronal excitability and synaptic dysfunction[76].

Although PD is considered a movement disorder, many patients experience non-motor symptoms too. As mentioned above, cognitive

decline and depression are among the clinical symptoms observed in PD patients during the later stages of the disease[37]. We found that hippocampal neurons harboring the *PINK1* and *PRKN* mutations have impaired electrophysiological properties, including reduced excitatory synaptic activity compared to the control hippocampal neurons and higher sodium currents in relatively mature neurons compared to the controls. The hippocampus plays a crucial role in cognition, including learning and memory[77]. In mouse models of *PINK1* and *PRKN* mutations, synaptic development and glutamatergic synaptic transmission were impaired in hippocampal neurons[78–80]. These alterations in synaptic activity in hippocampal neurons, as observed in our study, may contribute to the cognitive decline observed in the patients.

Moreover, we also observed that the hippocampal neurons derived from the patients with the *PINK1* and *PRKN* mutations had more pronounced calcium transients. Aging has been shown to increase the calcium transients in hippocampal neurons in rodent models[81,82]. Other studies also suggested changes in calcium homeostasis in hippocampal neurons that progress with aging, leading to alterations in synaptic strength (long-term depression and long-term potentiation)[83]. Evidence of elevated calcium signaling has also been demonstrated in mouse models of AD, resulting in neurite degeneration[84]. Furthermore, several studies have reported the biological role of *PINK1* and *PRKN* genes in mitochondrial biogenesis and trafficking[61,62] and the alteration in mitochondrial structure in hiPSC-derived neurons with *PINK1* and *PRKN* mutations[24]. Thus, we speculate that this alteration in calcium transients observed in a hippocampal neuron could be partly due to the effect of the mutation of *PINK1* and *PRKN* on mitochondria, as mitochondria play a crucial role in regulating calcium homeostasis[84–86]. Using mice models, Heeman et al. described *PINK1* depletion to be linked to a fragmentation of the mitochondrial network, mitochondrial membrane depolarization, and an increase in reactive oxygen species (ROS) production[87]. Thus, *PINK1* depletion affects mitochondrial metabolism, calcium homeostasis, and energy maintenance. Here, we had a unique opportunity to measure DA and hippocampal neurons from patients with mutations in both the *PINK1* and *PRKN* genes. The advantage of using a double mutant model (*PINK1* and *PRKN*) is that it allows us to explore these mutations' synergistic or additive effects on cellular function. On the other hand, the disadvantage of using a double mutant model is that it may be more challenging to dissect the individual contributions of each mutation to the observed phenotypes.

A study examining the effects of the *PRKN* mutation was recently published[41], but further studies are needed for a single mutant model of the *PINK1* gene to understand its distinct roles in the development and progression of PD. Increased calcium has been suggested to activate the calpain-mediated signaling pathways, which could affect learning and memory[83], and is also likely to indicate functional changes in hippocampal neurons before the appearance of neurodegeneration.

A few limitations should be noted for our study. The patients and controls have different genetic backgrounds, which may cause baseline differences between the samples. We utilized iPSC lines derived from two patients, one with a heterozygous and one with a homozygous *PINK1* mutation, both carrying a heterozygous *PRKN* mutation. When pooling these samples together, we can be more confident of the reported phenotypes, and it is essential to note that when evaluating the effects of the homozygous and heterozygous *PINK1* mutations separately, each mutation type is represented by a single sample. This distinction is crucial for interpreting our findings, as the unique genetic backgrounds and mutation types may influence the observed phenotypes. Therefore, conclusions drawn from our study should be considered with the understanding that further validation in a larger, more diverse cohort is necessary to generalize these results more broadly.

Furthermore, it is critical to consider the influence of sex and age on our study's outcomes. Our sample includes individuals of different age and sex, factors known to influence PD pathology and response to treatments. Notably, the patient samples were collected at the time of disease diagnosis, introducing a diversity in age and potentially in disease progression stages.

However, the application of iPSC technology in our study offers a unique advantage in addressing age-related variations. The process of reprogramming somatic cells into iPSCs is known to 'rejuvenate' the cells, effectively erasing age-related epigenetic markers[88]. This rejuvenation renders iPSC-derived neurons comparatively young, regardless of the donor's age at sample collection. This aspect is pivotal, as it suggests that the neurons derived from these iPSCs reflect a baseline state, minimizing the direct impact of age or environmental influence on our observations. Indeed, research has demonstrated that iPSC-derived neurons, regardless of the donor's age, exhibit similar gene expression profiles, electrophysiological properties, and phenotypic characteristics, supporting the robustness of this approach for modeling diseases like PD across a broad age range[89,90].

While this technology provides a critical tool for reducing variability associated with donor age, the inherent genetic diversity and the presence of heterozygous versus homozygous mutations necessitate a cautious interpretation of our findings. Each genetic configuration—coupled with the individual's sex—may contribute uniquely to the disease phenotype, underlining the importance of considering these factors when extrapolating our results to broader populations. Consequently, our study emphasizes the need for further investigation in more extensive, genetically, and demographically diverse cohorts to validate and extend our findings.

Additionally, as shown in Supplementary Fig. 3a, most of the neurons in the DA neuronal cultures were positive for TH (Tyrosine hydroxylase) (~90%), showing that they are DA neurons, and most of the neurons in the hippocampal cultures were positive for *PROX1*, showing that they are dentate gyrus granule hippocampal neurons (~70%). However, it is important to note that whole-cell patch-clamp experiments were performed on neurons based on their morphology (typically the larger neurons), but we did not have a reporter for the type of neuron that the experiment was performed on (RNA sequencing and whole-cell patch-clamp).

In conclusion, we conducted the first detailed functional study of dopaminergic and hippocampal neurons in hiPSC-derived neurons from PD patients with *PINK1* and *PRKN* double mutations and found alterations in electrophysiological properties as well as calcium homeostasis. These findings are also consistent with clinical symptoms found in PD patients and provide an exciting opportunity to use such hiPSC-based PD models as a preclinical drug-screening platform.

Methods

Ethics statement

The patients and healthy controls who participated in the study provided written informed consent. Ethics approval for the experiments in the study were obtained from the University of Haifa, reference number 282/22. Age and sex details for all cell lines utilized in this study are provided in Table 1.

iPSC generation

Skin biopsies were obtained and dissected to obtain human dermal fibroblasts. They were cultured in DMEM containing L-glutamine, 15% fetal bovine serum, NEAA, and sodium pyruvate with half of the media being replaced every two days[31,91]. Once the cells were confluent, they were trypsinized and 5×10^5 cells were subjected to transduction under feeder-free conditions using Yamanaka's reprogramming factors from the CytoTune®-iPSC2.0 Sendai Reprogramming Kit, Life Technologies, A16517. When the iPSC colonies reached a size suitable for picking, they were transferred onto geltrex-coated plates[31]. The pluripotency of the colonies was then confirmed through immunocytochemistry using TRA-1-60, SSEA4, Nanog, and OCT4 antibodies as shown in Supplementary Fig. 5.

DA neuron differentiation

To generate in vitro midbrain DA neurons, we employed a previously reported protocol[41,92]. HiPSCs obtained from two *PINK1* and *PRKN* patients and two healthy controls were grown until they became ~80% confluent. Accutase (AT104, Innovative Cell Technology) and trypsin inhibitor (10109886001, Sigma-Aldrich) were used to dissociate hiPSCs into a single-cell suspension, and the cells were then replated on matrigel-coated plates in mTesR plus media at a density of 40,000 cells/cm^2 (Stem Cell Technologies). Cells were allowed to proliferate for two days with a daily media change.

Table 1 | Description of patient-derived and control iPSC lines

Line	Type	Sex	Age	Data used	Mutations
iPSCDAneurons4	Control	Male	43	RNA seq	NA
iPSCDAneurons30	Control	Male	71	RNA seq, Ephys	NA
JEA16	Control	Male	53	Ephys	NA
Red ion	PD patient	Male	75	RNA seq, Ephys	PARK2 R275W/WT + PINK1 p.Try90Leu fs*12/WT
PP1	PD patient	Female	48	RNA seq, Ephys	homozygous PINK1 p.Try90Leufsx12+ het PARK2 Arg275Trp in exon 7

This table provides the details (age and sex) alongside the genetic characteristics of the patients and controls in the study. The mean age of control individuals was 56 ± 8 years (standard error). The mean age of PD patients was 61 ± 14 years (Standard error).

When the cells reached 70–80% confluency, the differentiation process was initiated by transferring to KSR media (DMEM F-12 (Biological industries, #01-170-1A) with Glutamax (35050-038, Gibco), 15% KO-SR (10828-010, Gibco), 1% NEAA (11140035, Gibco), 0.1 mM β-mercaptoethanol (219024280, MPB-MP Biomedicals)). The starting date of differentiation was designated as day 0. From day 5 to day 10, the medium was changed gradually to N2 medium (DMEM F-12 with Glutamax, 1% N2 supplement (17502-048, Gibco)) (for day 5 and 6: 75% KSR: 25% N2; whereas for day 7 and 8: 50% KSR: 50% N2; and for day 9 and 10: 25% KSR: 75% N2). The medium was changed to B27 medium on Day 11 (Neurobasal medium (NB; 21103049, Gibco), 2% B27 supplement, 1% glutamax, 10 ng/mL BDNF, 10 ng/mL GDNF (PHC7044, Gibco), 1 ng/mL TGFβ3 (100-36E, Peprotech), 0.2 mM ascorbic acid (5088177, Biogems), and 0.1 mM cAMP (1698950, Biogems)).

Throughout the differentiation process, small molecule components were introduced to the culture (10 M SB431542 (Cayman chemical company, #0573051-151) on days 0–4; 100 nM LDN-193189 (1066208, Biogems) on days 0–12; 2 M purmorphamine (biogems, #4831086) 0.25 M SAG (biogems, #9128694), 100 ng/mL FGF8b (100-25, Peprotech) on days 1–6; and 3 M CHIR99021 (biogems, #2520691) on days 3–12). After 20–25 days, neurons were dissociated and replated onto matrigel-coated coverslips and allowed to develop in the B27 medium until day 30. On day 30, the base medium was gradually replaced with Brainphys medium (Stem Cell Technologies, #05790) to induce synaptic connections. The whole-cell patch-clamp recording was performed on days 45–50.

Hippocampal differentiation

Additionally, we used a previously published strategy[93,94] to differentiate hiPSCs into hippocampal DG granule neurons. Similar to the differentiation of DA neurons, hiPSCs were grown to 80% confluency. Following this, embryoid bodies (EBs) were created by mechanically dissociating them with dispase; then they were plated onto low-adherence plates in an mTeSR plus media supplemented with Y-27632 ROCK inhibitor. For 20 days, the EBs were grown in an anti-caudalizing medium comprising DMEM/F12, Glutamax, B27 (without vitamin A) (12587-010, Gibco), N2, LDN-193189, XAV939, cyclopamine, and SB431542, followed by plating onto poly-ornithine/laminin (Sigma)-coated dishes in DMEM/F12 (Invitrogen) plus N2, B27 (without vitamin A) and laminin. After a week, rosettes were manually selected based on their morphology, dissociated with Accutase (Chemicon), plated onto poly-l-ornithine/laminin-coated plates, and fed with NPC media made up of the following ingredients: DMEM/F12, Glutamax, B27 (without vitamin A), N2, laminin, and FGF2. To differentiate the cells, ascorbic acid (200 nM), cyclic AMP (cAMP; 500 mg/ml), laminin (1 mg/ml), BDNF (20 ng/ml), and Wnt3a (20 ng/ml) were added to the differentiation medium for 14 days. Three weeks following the onset of the differentiation, the base medium was switched to BrainPhys.

Immunocytochemistry

Coverslips with DA and hippocampal DG granule neurons were fixed in warmed 4% paraformaldehyde (PFA) for 15 min. Following three washes with DPBS, the cells were then blocked and permeabilized in a blocking solution containing DPBS, 0.2% Molecular Grade Triton X-100, and 10% Donor Horse Serum for 60 min. Subsequently, we incubated the cells with primary antibodies in the blocking solution at 4 °C overnight, using the following antibodies at the stated dilutions for DA neurons: TH (1:500) and MAP2 (1:500), and for hippocampal neurons, PROX1 (1:4000) and MAP2 (1:500). On the next day, the coverslips were washed three times with DPBS (5 min each), incubated with the Alexa Fluor™ secondary antibodies and counterstained with DAPI staining solution (1:3000) for 60 min at room temperature. Then the coverslips were washed, mounted on slides using Fluoromount-G mounting medium (0100-01, Southern Biotech), and dried overnight in a dark box. The fluorescence signals were detected using a Nikon A1-R confocal microscope, and images were processed using NIS elements 5.21 (Nikon) and microscopy image analysis software Imaris 9.8 (Oxford Instruments).

RNA extraction, sequencing, and analyses

The total cellular RNA was extracted from 3 to 5 million DA neurons per sample that were derived from hiPSCs of two patients with *PINK1* and *PRKN* mutations and two lines of healthy controls at 7 to 8 weeks post-differentiation using the zymo RNA clean & concentrator kits, according to the manufacturer's instructions. Further, the RNA was reverse transcribed using the high-capacity cDNA synthesis kit from AB Biosystems. The RNA-Sequencing was performed on a NextSeq 500 sequencer. The average read length was 150 bp, and the average number of reads per sample was 10 million. The sequencing was performed using single-end reads. The experiment was conducted with two replicates for each of the patients and controls. These two biological replicates were grown separately. The traditional process for RNA-Sequencing data analysis includes creating FASTQ-format files containing reads sequenced on a next-generation sequencing (NGS) platform. FASTQC 14 v0.11.8 was used to check the quality of the sequenced reads, and STAR (ultrafast universal RNA-seq aligner algorithm) was used to align them to the hg38 human genome. Following this process, each gene's expression level was evaluated by counting the number of reads aligned to each exon or full-length transcript. The aligned sequences were counted and checked for differential expressions using HTSeq, a Python framework to work with high-throughput sequencing data, and DESeq2, a moderated estimation of fold change and dispersion for RNA-seq data. DEGs were determined using DESeq1 v.2.11.40.7, and the *p*-value was adjusted for multiple hypotheses with the Benjamini-Hochberg procedure[95], which controls for the false discovery rate (FDR). Genes with an FDR < 0.05 and |log2FC|>1.1 were included in the analysis. A Gene Ontology (GO) enrichment test and KEGG pathway analysis were performed using expressAnalyst.

A graphical representation of the protein network pathways analysis was constructed using nodes and edges, where each node represented a pathway connected by the edges (lines). The size of each node is proportional to the number of DEGs. An overrepresentation of GO terms and KEGG pathway was determined by FDR < 0.05. Edges between nodes indicate gene sets that share common genes, based on an overlap coefficient (OC) calculated by ExpressAnalyst. The OC is the average of the number of overlapping genes divided by the size of gene set 1 plus the number of overlapping genes divided by the size of gene set 2. An edge connects two gene sets if the OC is ≥0.3. The thickness of each edge represents the number

of genes shared between the two connected gene sets. Thicker edges denote a greater number of shared genes.

RT PCR

In this study, quantitative Real-Time PCR (qRT-PCR) was performed using the QuantStudio® 3 Real-Time PCR System (AB-A28571)and the SYBR® Green PCR Master Mix (Applied Biosystems, Catalog No. 4385612). 2 µg RNA was reverse transcribed into cDNA using the High-Capacity cDNA Reverse Transcription Kit (Applied Biosystems, Catalog No 4374966), following the manufacturer's protocol. The qRT-PCR reactions were conducted in a 20 µL mixture containing the synthesized cDNA, SYBR Green PCR Master Mix, and specific primers for GAPDH and four other target genes (primer sequences provided in the Supplementary Table 5). The thermal cycling conditions included an initial denaturation at 95 °C for 10 min, followed by 40 cycles of denaturation at 95 °C for 15 s, and a combined annealing and extension step at 60 °C for 1 min. Relative expression levels of the target genes were quantified using the 2^(-ΔΔCt) method, with GAPDH as an internal control. The data analysis was carried out using Microsoft excel.

Electrophysiology

Whole-cell patch-clamp recordings were performed on DA neurons derived from two PD patients carrying the *PINK1* and *PRKN* mutations and on DA neurons derived from two healthy controls after 45–50 days of differentiation. We differentiated the cells two to three separate times. In each time we recorded from at least two coverslips, and from each coverslip we typically recorded from five to seven neurons. Culture coverslips were placed inside a recording chamber that was filled with HEPES-based artificial cerebrospinal fluid (ACSF) containing (in mM) 139 NaCl, 10 HEPES, 4 KCl, 2 CaCl2, 10 D-glucose, and 1MgCl2 (pH 7.5, osmolarity adjusted to 310 mOsm) that had been warmed to 37 °C. The recording micropipettes (tip resistance of 10–15 MΩ) were filled with an internal solution containing (in mM) 130 K-gluconate, 6 KCl, 4 NaCl, 10 Na-HEPES, 0.2 K-EGTA, 0.3 GTP, 2 Mg-ATP, 0.2 cAMP, 10 D-glucose, 0.15% biocytin and 0.06% rhodamine (pH 7.5, osmolarity adjusted to 290–300 mOsm). Data were recorded at room temperature using Clampex v11.1 with a sampling rate of 20 kHz.

Electrophysiology analysis

For hippocampal neurons, we performed whole-cell patch clamp recordings at three different time points: two to four weeks (immature neurons, first-time point), six to eight weeks (young neurons, second-time point), and 8–11 weeks (mature neurons, third-time point).

Total evoked action potentials

Neurons were held in current clamp mode at −60 mV with a constant holding current. Following this, current injections were given in 3 pA stages over 400 ms, starting 12 pA below the steady-hold current needed for −60 mV membrane potential. A total of 38 depolarization steps were injected. Neurons that required more than 50 pA to maintain a voltage of −60 mV were excluded from the analysis. The total evoked action potential is the total number of action potentials that were counted in the first 30 (for hippocampal neurons) or 32 (for dopaminergic neurons) depolarization steps in 400 ms recordings.

Action potential shape analysis

The first evoked action potential (that was generated with the least amount of injected current) was used to examine the action potential shape in terms of spike fast after-hyperpolarization (fAHP), amplitude, width, and threshold. To compute the amplitude of the 5 ms fAHP, the difference between the spike threshold and the membrane potential value 5 ms after the potential returned to pass the threshold value at the end of the action potential, was used. The spike amplitude was determined as the difference between the highest membrane potential during a spike and the threshold. The time it took for the membrane potential to reach 50% of the spike's amplitude from the ascending to descending portion was used to compute the action potential width (Full Width at Half Maximum). The membrane potential known as the "spike threshold" occurs when a membrane potential depolarizes and its slope sharply increases, producing an action potential (the first maximum in the second derivative of the graph for voltage vs. time).

Analysis of sodium, fast and slow potassium currents

Current measurements for sodium and potassium were taken in voltage-clamp mode. Voltage steps of 400 ms in the range of −90 to 80 mV were produced while holding the cells at a voltage of −60 mV. The cell capacitance was used to normalize currents. The cell capacitance was acquired through a membrane test of the Clampex SW software. The maximal outgoing current that occurs right after a depolarization step, usually within a time range of a few milliseconds, was used to calculate the fast potassium current. The slow potassium current was taken as the current at the end of the 400 ms depolarization phase.

The sodium and potassium current amplitudes were statistically analyzed at specific test potentials (from −20 to 0 mV for sodium current and from 40 to 80 mV for potassium current). These specific potentials were chosen because they represent the physiological conditions of a healthy neuron.

Analysis of synaptic activity

In voltage-clamp mode, synaptic activity, i.e., spontaneous EPSC, was recorded. Currents in the patched neurons were monitored while the neurons were maintained at −60 mV. We evaluated the amplitude and rate of synaptic activity using custom-written Matlab code. The cumulative distribution of EPSCs amplitude was calculated for each group. For each cell, the rate of the synaptic activity was calculated by dividing the number of events by the length of the recording (non-active cells were also included, and the event rate was considered 0 for them).

Calcium imaging experiments and analyses

Calcium imaging was performed at two different time points for hippocampal neurons: initially at two to four weeks post-differentiation (first-time point) and later at six to seven weeks post-differentiation (second-time point).

To observe calcium transients, neuronal cells were incubated for an hour with 2 mM Fluo-5 AM in the ACSF, i.e., recording solution containing (in mM) 139 NaCl, 10 HEPES, 4 KCl, 2 CaCl2, 10 D-glucose, and 1MgCl2 (pH 7.5, osmolarity adjusted to 310 mOsm). After one hour of incubation, the culture coverslips were placed in a recording chamber filled with clean ACSF that had been pre-warmed to 37 °C, and imaging of calcium transients was performed with a video microscopy CCD digital camera (SciCam Pro, Scientifica). The images and data were captured and processed using a custom-written GUI in MATLAB 9.8 (R2021a, MathWorks).

A Python script was used to analyze the time series data for the calcium imaging recordings. Calcium transients' dynamics were examined to differentiate between neurons and astrocytes, which revealed unique activity patterns between the two types of cells. The astrocytes activity was attributed to the slow changes in calcium activity, whereas neurons showed fast transients. To analyze astrocytes and neurons separately, it was necessary to determine if the ROI contained an active neuron, an active astrocyte, or an inactive cell. The dynamic differences in fluorescence time series value were used to distinguish astrocytes from neurons.

We typically recorded 1800 frames. The frames were collected at ~10 Hz. To check the steepness of the rise of the fluorescence, we calculated the difference between the values of two adjacent frames. The differences Δf(n) between the current and n-6 samples were calculated and normalized by the maximum amplitude obtained over the entire recording period. If the maximum value of normalized Δf (t) exceeded the threshold of 0.05, it was labeled as an active neuron. Signals below the threshold were attributed to inactive cells or astrocytes.

An assessment to determine if ROIs were active astrocytes or inactive cells was performed on those not identified as active neurons. A fluorescence ratio (Δf/f0) was calculated for every signal by dividing the signal's maximum amplitude by the baseline fluorescence. The lowest value of the signal

was attributed as the baseline of the cell. The computed ratio was then compared to the ratio of the most active astrocyte (the astrocyte with the highest fluorescence ratio in a particular recorded area). The signal was considered inactive if its fluorescence ratio was less than 10% of the fluorescence ratio of the most active astrocyte. The remaining signals were characterized as active astrocytes.

The activity of neurons and astrocytes

A peak detection algorithm was used to count the fast calcium transient events of neurons. The lowest value of the signal was recorded as the baseline of the cell. The average baseline value for all cells was calculated. In addition, the fluorescence of the three most active astrocytes in a recording was averaged. The data were statistically tested and analyzed in Excel using the unpaired Student's *t* test (two-way).

Correlation calculations

Pairwise correlations were calculated for each ROI (one neuron), with each ROI over 35 samples (approximately 3.5 s). A moving average filter was used to calculate these correlations over the sampling time at each sampling point. These correlations were summed for a quantity that represents the correlation of the neuron with its surrounding neurons. The neurons were sorted according to this sum, and the average of the top 10 was obtained as a measure of synchronicity of this area in the recordings.

The power spectral density (PSD) ratio of all and high frequencies

The PSD is a valuable tool for analyzing the frequencies and amplitudes of oscillatory neurons. After sorting the neurons based on their event counts from selected high synchronized recordings, the PSD was calculated for each neuron, and the ratio of area under PSD for the full spectrum and the area under PSD for higher frequency components (greater than 0.1 Hz) was calculated. Then we calculated the mean of this ratio (all frequencies divided by high frequencies) for the top 10 neurons as a measure of this ratio of the area. We compared this ratio of area under the curve for the topmost correlated five ROIs and calculated the mean correlation according to these chosen ROIs.

Statistical analyses

Statistical tests for electrophysiology data were performed using Clampfit-11.1 and Matlab software (R2021a, The MathWorks Inc., Natick, MA, 2000). The *p*-values were calculated using a two-sample t-test (two-tailed) unless otherwise mentioned (such as the Welch-correction test for comparison of the spike amplitude in DA neurons and Mann–Whitney test for comparing evoked potential in heterozygous and homozygous *PINK1* mutant). The sodium and potassium current changes were analyzed using one-way ANOVA analysis. All data values were presented as mean ± standard error (SE). A value of $p < 0.05$ was considered significant for all statistical tests. For RNA sequencing analysis, the FDR-adjusted mean value was evaluated, and a FDR < 0.05 was considered significant.

Data availability

The data used in this study are available upon request to the corresponding author. Please contact Shani Stern at sstern@unive.haifa.ac.il for access to the whole cell patch clamp data. The RNA sequencing data have been deposited to the NCBI repository (BioProject accession number PRJNA1054046).

Code availability

The data analysis code used in this study are available upon request to the corresponding author.

Received: 8 January 2023; Accepted: 25 April 2024;
Published online: 18 May 2024

References

1. Lajoie, A. C., Lafontaine, A.-L. & Kaminska, M. The Spectrum of Sleep Disorders in Parkinson Disease: A Review. *Chest* **159**, 818–827 (2021).
2. Poewe, W. et al. Parkinson disease. *Nat. Rev. Dis. Primer* **3**, 17013 (2017).
3. Chao, T.-K., Hu, J. & Pringsheim, T. Risk factors for the onset and progression of Huntington disease. *NeuroToxicology* **61**, 79–99 (2017).
4. Guerreiro, R. & Bras, J. The age factor in Alzheimer's disease. *Genome Med.* **7**, 106 (2015).
5. Mizrahi, L., Shekhidem, H. A. & Stern, S. Age separation dramatically reduces COVID-19 mortality rate in a computational model of a large population. *Open Biol*. **10**, 200213 (2020).
6. Niccoli, T., Partridge, L. & Isaacs, A. M. Ageing as a risk factor for ALS/FTD. *Hum. Mol. Genet.* **26**, R105–R113 (2017).
7. Deng, H., Wang, P. & Jankovic, J. The genetics of Parkinson disease. *Ageing Res. Rev.* **42**, 72–85 (2018).
8. Domingo, A. & Klein, C. Genetics of Parkinson disease. *Handb. Clin. Neurol.* **147**, 211–227 (2018).
9. Tysnes, O.-B. & Storstein, A. Epidemiology of Parkinson's disease. *J. Neural Transm. Vienna Austria 1996* **124**, 901–905 (2017).
10. Langley, J., Huddleston, D. E., Sedlacik, J., Boelmans, K. & Hu, X. P. Parkinson's disease–related increase of -weighted hypointensity in substantia nigra pars compacta. *Mov. Disord.* **32**, 441–449 (2017).
11. Lemprière, S. Exosomal α-synuclein as a biomarker for Parkinson disease. *Nat. Rev. Neurol.* **16**, 242–243 (2020).
12. Espay, A. J. et al. Disease modification and biomarker development in Parkinson disease: Revision or reconstruction? *Neurology* **94**, 481–494 (2020).
13. Balestrino, R. & Schapira, A. H. V. Parkinson disease. *Eur. J. Neurol.* **27**, 27–42 (2020).
14. Barnhill, L. M., Murata, H. & Bronstein, J. M. Studying the Pathophysiology of Parkinson's Disease Using Zebrafish. *Biomedicines* **8**, E197 (2020).
15. Mellick, G. D. et al. Screening PARK genes for mutations in early-onset Parkinson's disease patients from Queensland, Australia. *Parkinsonism Relat. Disord.* **15**, 105–109 (2009).
16. Sironi, F. et al. Parkin analysis in early onset Parkinson's disease. *Parkinsonism Relat. Disord.* **14**, 326–333 (2008).
17. Kitada, T. et al. Mutations in the parkin gene cause autosomal recessive juvenile parkinsonism. *Nature* **392**, 605–608 (1998).
18. Tanaka, K. The PINK1-Parkin axis: An Overview. *Neurosci. Res.* **159**, 9–15 (2020).
19. Spratt, D. E. et al. A molecular explanation for the recessive nature of parkin-linked Parkinson's disease. *Nat. Commun.* **4**, 1983 (2013).
20. Sekine, S. PINK1 import regulation at a crossroad of mitochondrial fate: the molecular mechanisms of PINK1 import. *J. Biochem.* **167**, 217–224 (2020).
21. Ibáñez, P. et al. Mutational analysis of the PINK1 gene in early-onset parkinsonism in Europe and North Africa. *Brain*. *J. Neurol.* **129**, 686–694 (2006).
22. Ishihara-Paul, L. et al. PINK1 mutations and parkinsonism. *Neurology* **71**, 896–902 (2008).
23. Bader, V. & Winklhofer, K. F. PINK1 and Parkin: team players in stress-induced mitophagy. *Biol. Chem.* **401**, 891–899 (2020).
24. Chung, S. Y. et al. Parkin and PINK1 Patient iPSC-Derived Midbrain Dopamine Neurons Exhibit Mitochondrial Dysfunction and α-Synuclein Accumulation. *Stem Cell Rep.* **7**, 664–677 (2016).
25. Marton, R. M. & Ioannidis, J. P. A. A Comprehensive Analysis of Protocols for Deriving Dopaminergic Neurons from Human Pluripotent Stem Cells. *Stem Cells Transl. Med.* **8**, 366–374 (2019).
26. Wang, M., Ling, K.-H., Tan, J. J. & Lu, C.-B. Development and Differentiation of Midbrain Dopaminergic Neuron: From Bench to Bedside. *Cells* **9**, E1489 (2020).
27. Brant, B. et al. IQSEC2 mutation associated with epilepsy, intellectual disability, and autism results in hyperexcitability of patient-derived neurons and deficient synaptic transmission. *Mol. Psychiatry* **26**, 7498–7508 (2021).

28. Stern, S. et al. A Physiological Instability Displayed in Hippocampal Neurons Derived From Lithium-Nonresponsive Bipolar Disorder Patients. *Biol. Psychiatry* **88**, 150–158 (2020).
29. Schafer, S. T. et al. Pathological priming causes developmental gene network heterochronicity in autistic subject-derived neurons. *Nat. Neurosci.* **22**, 243–255 (2019).
30. Choudhary A, Peles D, Nayak R, Mizrahi L, Stern S. Current progress in understanding schizophrenia using genomics and pluripotent stem cells: A meta-analytical overview. Schizophr Res. S0920-9964(22)00406-6 (2022). https://doi.org/10.1016/j.schres.2022.11.001.
31. Mertens, J. et al. Age-dependent instability of mature neuronal fate in induced neurons from Alzheimer's patients. *Cell Stem Cell* **28**, 1533–1548.e6 (2021).
32. Fujimori, K. et al. Modeling sporadic ALS in iPSC-derived motor neurons identifies a potential therapeutic agent. *Nat. Med.* **24**, 1579–1589 (2018).
33. Avior, Y. et al. Depression patient-derived cortical neurons reveal potential biomarkers for antidepressant response. *Transl. Psychiatry* **11**, 1–10 (2021).
34. Penney, J., Ralvenius, W. T. & Tsai, L.-H. Modeling Alzheimer's disease with iPSC-derived brain cells. *Mol. Psychiatry* **25**, 148–167 (2020).
35. Avazzadeh, S., Baena, J. M., Keighron, C., Feller-Sanchez, Y. & Quinlan, L. R. Modelling Parkinson's Disease: iPSCs towards Better Understanding of Human Pathology. *Brain Sci.* **11**, 373 (2021).
36. Hu, X. et al. Modeling Parkinson's Disease Using Induced Pluripotent Stem Cells. *Stem Cells Int.* **2020**, 1061470 (2020).
37. Barbosa, E. R. Non-motor symptoms in Parkinson's disease. *Arq. Neuropsiquiatr.* **71**, 203–204 (2013).
38. Sawyer, K., Corsentino, E., Sachs-Ericsson, N. & Steffens, D. C. Depression, hippocampal volume changes, and cognitive decline in a clinical sample of older depressed outpatients and non-depressed controls. *Aging Ment. Health* **16**, 753–762 (2012).
39. Toda, T., Parylak, S. L., Linker, S. B. & Gage, F. H. The role of adult hippocampal neurogenesis in brain health and disease. *Mol. Psychiatry* **24**, 67–87 (2019).
40. Lim, J., Bang, Y. & Choi, H. J. Abnormal hippocampal neurogenesis in Parkinson's disease: relevance to a new therapeutic target for depression with Parkinson's disease. *Arch. Pharm. Res.* **41**, 943–954 (2018).
41. Stern, S. et al. Reduced Synaptic Activity and Dysregulated Extracellular Matrix Pathways Are Common Phenotypes in Midbrain Neurons Derived from Sporadic and Mutation-Associated Parkinson's Disease Patients. https://doi.org/10.1101/2021.12.31.474654 (2022)
42. Kerrisk, M. E., Cingolani, L. A. & Koleske, A. J. ECM receptors in neuronal structure, synaptic plasticity, and behavior. *Prog. Brain Res.* **214**, 101–131 (2014).
43. Ferrer-Ferrer, M. & Dityatev, A. Shaping Synapses by the Neural Extracellular Matrix. *Front. Neuroanat.* **12**, 40 (2018).
44. Navarro, A. I. & Rico, B. Focal adhesion kinase function in neuronal development. *Curr. Opin. Neurobiol.* **27**, 89–95 (2014).
45. Valiente, M., Ciceri, G., Rico, B. & Marín, O. Focal adhesion kinase modulates radial glia-dependent neuronal migration through connexin-26. *J. Neurosci. Off. J. Soc. Neurosci.* **31**, 11678–11691 (2011).
46. Kuga, N., Sasaki, T., Takahara, Y., Matsuki, N. & Ikegaya, Y. Large-Scale Calcium Waves Traveling through Astrocytic Networks In Vivo. *J. Neurosci.* **31**, 2607–2614 (2011).
47. Scemes, E. & Giaume, C. Astrocyte Calcium Waves. *Glia* **54**, 716–725 (2006).
48. Kanemaru, K. et al. In Vivo Visualization of Subtle, Transient, and Local Activity of Astrocytes Using an Ultrasensitive Ca2+ Indicator. *Cell Rep.* **8**, 311–318 (2014).
49. Tran, J., Anastacio, H. & Bardy, C. Genetic predispositions of Parkinson's disease revealed in patient-derived brain cells. *NPJ Park. Dis.* **6**, 8 (2020).
50. Braak, H. et al. Staging of brain pathology related to sporadic Parkinson's disease. *Neurobiol. Aging* **24**, 197–211 (2003).
51. Del Tredici, K. & Braak, H. Review: Sporadic Parkinson's disease: development and distribution of α-synuclein pathology. *Neuropathol. Appl. Neurobiol.* **42**, 33–50 (2016).
52. Madeo, G. et al. PINK1 heterozygous mutations induce subtle alterations in dopamine-dependent synaptic plasticity. *Mov. Disord. Off. J. Mov. Disord. Soc.* **29**, 41–53 (2014).
53. Kitada, T. et al. Impaired dopamine release and synaptic plasticity in the striatum of PINK1-deficient mice. *Proc. Natl. Acad. Sci. USA.* **104**, 11441–11446 (2007).
54. Paillé, V. et al. Distinct levels of dopamine denervation differentially alter striatal synaptic plasticity and NMDA receptor subunit composition. *J. Neurosci. Off. J. Soc. Neurosci.* **30**, 14182–14193 (2010).
55. Matikainen-Ankney, B. A. et al. Altered Development of Synapse Structure and Function in Striatum Caused by Parkinson's Disease-Linked LRRK2-G2019S Mutation. *J. Neurosci. Off. J. Soc. Neurosci.* **36**, 7128–7141 (2016).
56. García-Junco-Clemente, P. et al. Cysteine string protein-alpha prevents activity-dependent degeneration in GABAergic synapses. *J. Neurosci. Off. J. Soc. Neurosci.* **30**, 7377–7391 (2010).
57. Bellucci, A. et al. Review: Parkinson's disease: from synaptic loss to connectome dysfunction. *Neuropathol. Appl. Neurobiol.* **42**, 77–94 (2016).
58. Picconi, B., Piccoli, G. & Calabresi, P. Synaptic Dysfunction in Parkinson's Disease. In *Synaptic Plasticity: Dynamics, Development and Disease* (eds. Kreutz, M. R. & Sala, C.) 553–572 (Springer, 2012). https://doi.org/10.1007/978-3-7091-0932-8_24.
59. Merlo, S., Spampinato, S. F. & Sortino, M. A. Early compensatory responses against neuronal injury: A new therapeutic window of opportunity for Alzheimer's Disease? *CNS Neurosci. Ther.* **25**, 5–13 (2019).
60. Hussein, Y. et al. Early maturation and hyperexcitability is a shared phenotype of cortical neurons derived from different ASD-associated mutations. *Transl. Psychiatry* **13**, 246 (2023).
61. Smith, K. M. & Dahodwala, N. Gender differences in Parkinson's disease and other movement disorders. *Exp. Neurol.* **259**, 44–56 (2014).
62. Sethi, M. K. & Zaia, J. Extracellular matrix proteomics in schizophrenia and Alzheimer's disease. *Anal. Bioanal. Chem.* **409**, 379–394 (2017).
63. Koskinen, M.-K., van Mourik, Y., Smit, A. B., Riga, D. & Spijker, S. From stress to depression: development of extracellular matrix-dependent cognitive impairment following social stress. *Sci. Rep.* **10**, 17308 (2020).
64. Jung, S. et al. Decreased expression of extracellular matrix proteins and trophic factors in the amygdala complex of depressed mice after chronic immobilization stress. *BMC Neurosci.* **13**, 58 (2012).
65. Zhang, H. et al. Reelin gene alleles and susceptibility to autism spectrum disorders. *Mol. Psychiatry* **7**, 1012–1017 (2002).
66. Dwyer, C. A. & Esko, J. D. Glycan susceptibility factors in autism spectrum disorders. *Mol. Aspects Med.* **51**, 104–114 (2016).
67. Wu, C. Focal adhesion: a focal point in current cell biology and molecular medicine. *Cell Adhes. Migr.* **1**, 13–18 (2007).
68. Caltagarone, J., Jing, Z. & Bowser, R. Focal adhesions regulate Abeta signaling and cell death in Alzheimer's disease. *Biochim. Biophys. Acta* **1772**, 438–445 (2007).
69. Schaefer, A. M., Taylor, R. W., Turnbull, D. M. & Chinnery, P. F. The epidemiology of mitochondrial disorders—past, present and future. *Biochim. Biophys. Acta BBA Bioenerg.* **1659**, 115–120 (2004).
70. Maltecca, F. et al. The Mitochondrial Protease AFG3L2 Is Essential for Axonal Development. *J. Neurosci.* **28**, 2827–2836 (2008).

71. Xiao, Y. et al. Targeting Glutamine Metabolism as an Attractive Therapeutic Strategy for Acute Myeloid Leukemia. *Curr. Treat. Options Oncol.* **24**, 1021–1035 (2023).
72. Meldrum, B. S. Glutamate as a Neurotransmitter in the Brain: Review of Physiology and Pathology. *J. Nutr.* **130**, 1007S–1015S (2000).
73. Natarajan, S. K. & Venneti, S. Glutamine Metabolism in Brain Tumors. *Cancers* **11**, 1628 (2019).
74. Esposti, M. D. The roles of Bid. *APOPTOSIS* **7**, 433–440 (2002).
75. Monzio Compagnoni, G. et al. The Role of Mitochondria in Neurodegenerative Diseases: the Lesson from Alzheimer's Disease and Parkinson's Disease. *Mol. Neurobiol.* **57**, 2959–2980 (2020).
76. Exner, N., Lutz, A. K., Haass, C. & Winklhofer, K. F. Mitochondrial dysfunction in Parkinson's disease: molecular mechanisms and pathophysiological consequences: Mitochondrial dysfunction in Parkinson's disease. *EMBO J.* **31**, 3038–3062 (2012).
77. O'Shea, A., Cohen, R. A., Porges, E. C., Nissim, N. R. & Woods, A. J. Cognitive Aging and the Hippocampus in Older Adults. *Front. Aging Neurosci.* **8**, 298 (2016).
78. Zhu, M., Cortese, G. P. & Waites, C. L. Parkinson's disease-linked Parkin mutations impair glutamatergic signaling in hippocampal neurons. *BMC Biol.* **16**, 100 (2018).
79. Gao, Q. et al. PINK1-mediated Drp1S616 phosphorylation modulates synaptic development and plasticity via promoting mitochondrial fission. *Signal Transduct. Target. Ther.* **7**, 103 (2022).
80. Feligioni, M. et al. Subtle alterations of excitatory transmission are linked to presynaptic changes in the hippocampus of PINK1-deficient mice. *Synapse* **70**, 223–230 (2016).
81. Toescu, E. C. & Verkhratsky, A. The importance of being subtle: small changes in calcium homeostasis control cognitive decline in normal aging. *Aging Cell* **6**, 267–273 (2007).
82. Gant, J. C., Sama, M. M., Landfield, P. W. & Thibault, O. Early and Simultaneous Emergence of Multiple Hippocampal Biomarkers of Aging Is Mediated by Ca2+-Induced Ca2+ Release. *J. Neurosci.* **26**, 3482–3490 (2006).
83. Foster, T. C. Calcium homeostasis and modulation of synaptic plasticity in the aged brain. *Aging Cell* **6**, 319–325 (2007).
84. Bezprozvanny, I. Calcium signaling and neurodegenerative diseases. *Trends Mol. Med.* **15**, 89–100 (2009).
85. Deas, E., Plun-Favreau, H. & Wood, N. W. PINK1 function in health and disease. *EMBO Mol. Med.* **1**, 152–165 (2009).
86. Yu, W., Sun, Y., Guo, S. & Lu, B. The PINK1/Parkin pathway regulates mitochondrial dynamics and function in mammalian hippocampal and dopaminergic neurons. *Hum. Mol. Genet.* **20**, 3227–3240 (2011).
87. Heeman, B. et al. Depletion of PINK1 affects mitochondrial metabolism, calcium homeostasis and energy maintenance. *J. Cell Sci.* **124**, 1115–1125 (2011).
88. Lapasset, L. et al. Rejuvenating senescent and centenarian human cells by reprogramming through the pluripotent state. *Genes Dev.* **25**, 2248–2253 (2011).
89. Miller, J. D. et al. Human iPSC-Based Modeling of Late-Onset Disease via Progerin-Induced Aging. *Cell Stem Cell* **13**, 691–705 (2013).
90. Mertens, J. et al. Directly Reprogrammed Human Neurons Retain Aging-Associated Transcriptomic Signatures and Reveal Age-Related Nucleocytoplasmic Defects. *Cell Stem Cell* **17**, 705–718 (2015).
91. Nayak, R. et al. Generation and characterization of iPSC lines (UOHi003-A, UOHi002-A) from a patient with SHANK3 mutation and her healthy mother. *Stem Cell Res.* **64**, 102899 (2022).
92. Kriks, S. et al. Dopamine neurons derived from human ES cells efficiently engraft in animal models of Parkinson's disease. *Nature* **480**, 547–551 (2011).
93. Yu, D. X., Marchetto, M. C. & Gage, F. H. How to make a hippocampal dentate gyrus granule neuron. *Dev. Camb. Engl.* **141**, 2366–2375 (2014).
94. Stern, S. et al. Neurons derived from patients with bipolar disorder divide into intrinsically different sub-populations of neurons, predicting the patients' responsiveness to lithium. *Mol. Psychiatry* **23**, 1453–1465 (2018).
95. Benjamini, Y. & Hochberg, Y. Controlling the False Discovery Rate: A Practical and Powerful Approach to Multiple Testing. *J. R. Stat. Soc. Ser. B Methodol.* **57**, 289–300 (1995).

Acknowledgements

The authors would like to thank the Israel Science Foundation (ISF grant 1994/21 and 3252/21) and Zuckerman (Zuckerman STEM leadership program) to S.S. and the JPB foundation to F.H.G. for funding and support. We also extend our gratitude to the patients for their participation and to the NIHR UCLH Biomedical Research Centre and the Queen Square Bioresource for their support. Additionally, we acknowledge the support of the AHA/Allen grant: AHA-Allen Initiative in Brain Health and Cognitive Impairment award made jointly through the American Heart Association and The Paul G. Allen Frontiers Group: 19PABH134610000, granted to F.H.G.

Author contributions

Utkarsh Tripathi wrote the manuscript and grew cells, performed patch clamp, calcium imaging, calcium imaging analysis, and analyzed all whole cell patch clamp data. Idan Rosh conducted whole-cell patch clamp experiments and cell cultures. Shani Stern designed the experiments, performed patch clamp analysis, produced the neural progenitor cells, wrote the Matlab scripts, and edited the manuscript. Fred H. Gage designed the experiments and edited the manuscript. Andreea Manole and Henry Haulden obtained the patient's cohorts. Jose Djamus performed cell culture and differentiation. Ritu Nayak contributed to neuronal differentiation and did proof-reading. Yara Hussein performed immunostaining for all the cultures. Ashwani Choudhary performed RT-qPCR experiments and assisted in manuscript preparation. Ran Ben Ezer analyzed RNA sequencing data. All authors approved the final version of the manuscript.

Competing interests

The authors declare no competing interests.

Additional information

Supplementary information The online version contains supplementary material available at https://doi.org/10.1038/s41531-024-00715-0.

Correspondence and requests for materials should be addressed to Shani Stern.